

Are we witnessing the epoch of reionization at $z = 7.1$ from the spectrum of J1120+0641?

Bradley Greig,¹★ Andrei Mesinger,¹ Zoltán Haiman² and Robert A. Simcoe^{3,4}

¹*Scuola Normale Superiore, Piazza dei Cavalieri 7, I-56126 Pisa, Italy*

²*Department of Astronomy, Columbia University, 550 West 120th Street, New York, NY 10027, USA*

³*Massachusetts Institute of Technology, 77 Massachusetts Ave, Cambridge, MA 02139, USA*

⁴*MIT-Kavli Center for Astrophysics and Space Research, Cambridge, MA 02109, USA*

Accepted 2016 December 21. Received 2016 December 21; in original form 2016 May 30

ABSTRACT

We quantify the presence of Ly α damping wing absorption from a partially neutral intergalactic medium (IGM) in the spectrum of the $z = 7.08$ QSO, ULASJ1120+0641. Using a Bayesian framework, we simultaneously account for uncertainties in: (i) the intrinsic QSO emission spectrum; and (ii) the distribution of cosmic H I patches during the epoch of reionization (EoR). For (i), we use a new intrinsic Ly α emission line reconstruction method, sampling a covariance matrix of emission line properties built from a large data base of moderate- z QSOs. For (ii), we use the Evolution of 21-cm Structure (EOS; Mesinger et al.) simulations, which span a range of physically motivated EoR models. We find strong evidence for the presence of damping wing absorption redward of Ly α (where there is no contamination from the Ly α forest). Our analysis implies that the EoR is not yet complete by $z = 7.1$, with the volume-weighted IGM neutral fraction constrained to $\bar{x}_{\text{H I}} = 0.40^{+0.21}_{-0.19}$ at 1σ ($\bar{x}_{\text{H I}} = 0.40^{+0.41}_{-0.32}$ at 2σ). This result is insensitive to the EoR morphology. Our detection of significant neutral H I in the IGM at $z = 7.1$ is consistent with the latest *Planck* 2016 measurements of the CMB Thompson scattering optical depth.

Key words: quasars: emission lines – quasars: general – cosmology: observations – cosmology: theory – dark ages, reionization, first stars.

1 INTRODUCTION

The epoch of reionization (EoR) signals the end of the cosmic dark ages, when ionizing radiation from the first stars and galaxies spreads throughout the Universe, beginning the last major baryonic phase change. This EoR is rich in astrophysical information, providing insights into the formation, properties and evolution of the first cosmic structures in the Universe.

Several recent $z \gtrsim 6$ observations have provided (controversial) information about the EoR (for a review, see e.g. Mesinger 2016). These come either from integral constraints on H II provided by the Thomson scattering of Cosmic Microwave Background (CMB) photons (e.g. George et al. 2015; Planck Collaboration XIII 2016), or Ly α absorption by putative cosmic H I patches along the lines of sight towards $z \lesssim 6$ objects. Since the cross-section at the Ly α line centre is large enough to saturate transmission even in the ionized intergalactic medium (IGM; requiring only trace values of neutral hydrogen: $x_{\text{H I}} \lesssim 10^{-4} - 10^{-5}$), the latter constraints generally rely on the damping wing of the line. The relative flatness of the damping wing with frequency contributes a smooth absorption

profile, which can result in optical depths of order a few during the EoR at frequencies around the redshifted Ly α line.

For galaxies, constraining damping wing absorption must be done with large samples, using their redshift evolution and/or clustering properties (e.g. Haiman & Spaans 1999; Ouchi et al. 2010; Stark et al. 2010; Pentericci 2011; Ono et al. 2012; Caruana et al. 2014; Schenker et al. 2014). QSOs however can be much brighter, allowing the detection of the EoR damping wing from a single spectrum. Most bright $z \lesssim 6$ QSOs have a large region of detectable flux blueward of the rest frame 1216 Å, where the flux from the QSO itself is thought to facilitate transmission even for photons redshifting into the Ly α resonant core. If this so-called near zone is large, then the imprint of an EoR damping wing can be isolated as a smooth absorption component on top of the fluctuating resonant absorption (the Ly α forest) inside the near zone (e.g. Mesinger, Haiman & Cen 2004; Bolton & Haehnelt 2007a,b; Schroeder, Mesinger & Haiman 2013). The intrinsic (unabsorbed) Ly α line profile can be reconstructed from the red side of the line (where absorption is minimal), assuming that the line is symmetric (a reasonable assumption for bright QSOs; e.g. Kramer & Haiman 2009). However, one is faced with the challenge of modelling the statistics of the Ly α forest in the near zone, which depends on the ionizing background and temperature.

The highest redshift QSO observed to date, the $z \sim 7.1$ object ULASJ1120+0641 (Mortlock et al. 2011, hereafter ULASJ1120),

★E-mail: bradley.greig@sns.it

appears to have an uncharacteristically small near zone: ~ 2 proper Mpc, roughly a factor of 3 to 4 smaller than generally found in $z \sim 6$ QSOs of comparable brightness (Carilli et al. 2010).¹ If the IGM is indeed undergoing reionization at $z = 7.1$, cosmic H I patches along the line of sight could be close enough to the quasar to imprint a detectable damping wing signature away from the near zone edge, even redward of the Ly α emission line centre.² Redward of the Ly α line centre (and redward of any redshifted cosmological infall; e.g. Barkana & Loeb 2004), there is no contribution from resonant absorption in the Ly α forest (see Section 2.3). Not having to model the Ly α forest simplifies the analysis considerably. However, as it might contain a damping wing imprint, the red side of the observed emission line can no longer be used to independently reconstruct the Ly α line profile. Moreover, the intrinsic Ly α emission profile can vary significantly from object to object, complicating the usefulness of a composite emission template. Thus, *any analysis of the IGM damping wing would need to fold-in the significant uncertainties in the shape and amplitude of the intrinsic Ly α line profile.*

The difficulty in reconstructing the intrinsic emission of ULASJ1120 is further exacerbated by its peculiar emission line features. Mortlock et al. (2011) report an extremely large C IV blueshift relative to its systemic redshift, which is larger than what has been observed in 99.9 per cent of all known QSOs. Bosman & Becker (2015) recently suggested that the observed Ly α emission of ULASJ1120 might be consistent with the subsample of objects with similar C IV properties, potentially alleviating the need for additional damping wing absorption.³ Correctly accounting for correlations of line properties is therefore critical for any robust claims on reionization from ULASJ1120.

In this work, we re-analyse the spectrum of ULASJ1120, improving on prior work with a combination of the following:

(i) We use the recently developed intrinsic Ly α emission line reconstruction method (Greig et al. 2016), which samples a covariance matrix of emission line properties from ~ 1500 moderate- z unobscured QSOs.

(ii) We use the latest, large-scale (1.6 Gpc on a side), physics-rich simulations of the EoR (Mesinger, Greig, & Sobacchi 2017) to extract 10^5 sightlines of opacity from $\sim 10^{12} M_{\odot}$ haloes (typical of bright QSOs; e.g. Fan et al. 2006; Mortlock et al. 2011).

(iii) We fold all uncertainties into a Bayesian framework, recovering robust constraints on the IGM neutral fraction at $z = 7.1$, which, for the first time, include rigorous statistical confidence intervals.

The remainder of this paper is organized as follows. In Section 2.1, we summarize the key components of the intrinsic Ly α reconstruction method, the observed spectrum of ULASJ1120 to be used in this analysis, and the recovery of the reconstructed Ly α line profile. In Section 2.2, we discuss the semi-numerical reionization simulations and the extraction of the synthetic damping wing profiles and, in Section 2.3, we outline our combined analysis. In Section 3, we discuss the constraints on the IGM neutral fraction resulting from the imprint of the IGM damping wing, and in Section 4, we consider the possibility of a DLA contributing the damping wing imprint. Finally, in Section 5, we finish with our closing remarks. Throughout this work, we adopt the background cosmological parameters: $(\Omega_{\Lambda}, \Omega_M, \Omega_b, n, \sigma_8, H_0) = (0.69, 0.31, 0.048, 0.97, 0.81, 68 \text{ km s}^{-1} \text{ Mpc}^{-1})$, consistent with cosmic microwave background anisotropy measurements by the *Planck* satellite (Planck Collaboration XIII 2016) and unless otherwise stated, distances are quoted in comoving units.

2 METHOD

2.1 Reconstruction of the intrinsic Ly α profile

The analysis of the IGM damping wing imprint within the spectrum of ULASJ1120 hinges on the recovery of the intrinsic Ly α emission line profile. Already, in the previous section, we have alluded to the difficulties in applying a QSO composite template to ULASJ1120. Within this work, we utilize the recently developed covariance matrix method of Greig et al. (2016) to obtain our reconstructed estimate of the intrinsic Ly α emission line profile.⁴

In this work, we make use of the Simcoe et al. (2012) ULASJ1120 spectrum, obtained from the FIRE infrared spectrometer (Simcoe et al. 2008) on the Magellan/Baade telescope. This spectrum offers an order of magnitude improvement in spatial (frequency) resolution compared to the Mortlock et al. (2011) discovery spectrum, with a similar signal-to-noise ratio (S/N).⁵ Throughout this work, we report all results in the QSO rest frame, with which we convert from the observed frame using the atomic [C II] transition. The resulting ULASJ1120 redshift is $z = 7.0842 \pm 0.0004$ (Venemans et al. 2012).⁶

¹ Note that quantitative EoR constraints using just the apparent size of the near zone require assumptions about the QSO age, environment, and ionization history (e.g. Mesinger et al. 2004; Maselli et al. 2007; Bolton et al. 2011).

² In principle, strong Ly α attenuation could also be caused by a damped Ly α absorber (DLA) intersected along the line of sight. However, such a system would have to have both an extremely high column density [$\log_{10}(N_{\text{H I}}/\text{cm}^{-2}) = 20.5 - 21$; Simcoe et al. 2012; Schroeder et al. 2013] and an extremely low metallicity ($Z \lesssim 10^{-4} Z_{\odot}$; e.g. Simcoe et al. 2012; Maio, Ciardi & Müller 2013). As we discuss further below, the number density of such objects in a random IGM sightline is extremely small (e.g. Prochaska & Wolfe 2009).

³ Note that the samples of SDSS QSOs used in the Bosman & Becker (2015) analysis are selected purely on their C IV equivalent width and the velocity offset of the C IV emission line relative to the C IV emission line of ULASJ1120+0641. Therefore, they are not necessarily selecting anomalous QSOs like ULASJ1120. Furthermore, these SDSS QSOs use only the C III] line for the redshift determination. The C III] line complex is a blend of several emission lines (Al III, Si III], and C III]) and as a result the contributions from the different individual line profiles may lead to small biases in their determined velocity offsets.

⁴ An alternative approach could be to reconstruct a template using a principal component analysis (PCA; e.g. Boroson & Green 1992; Francis et al. 1992; Suzuki et al. 2005; Suzuki 2006; Lee & Spergel 2011; Pâris et al. 2011; Simcoe et al. 2012). However, typically this is used for characterizing the mean QSO composite obtained from fits to the full QSO spectrum with the fewest eigenvectors. How well this approach would work in reconstructing the intrinsic profile of Ly α , and characterizing the properties of an individual source as peculiar as ULASJ1120, is beyond the scope of this work.

⁵ In order to test the robustness of our fit to ULASJ1120, we additionally performed our MCMC fitting approach on the Mortlock et al. (2011) discovery spectrum. While this spectrum has an order of magnitude lower resolution, this should not impact the recovery of the strong high-ionization lines. Not shown here, we confirm that indeed we do recover similar fits for all emission line features.

⁶ The uncertainty on the redshift determination is implicitly accounted for within our MCMC fitting approach, by allowing the velocity offset of each individual emission line to be a free parameter.

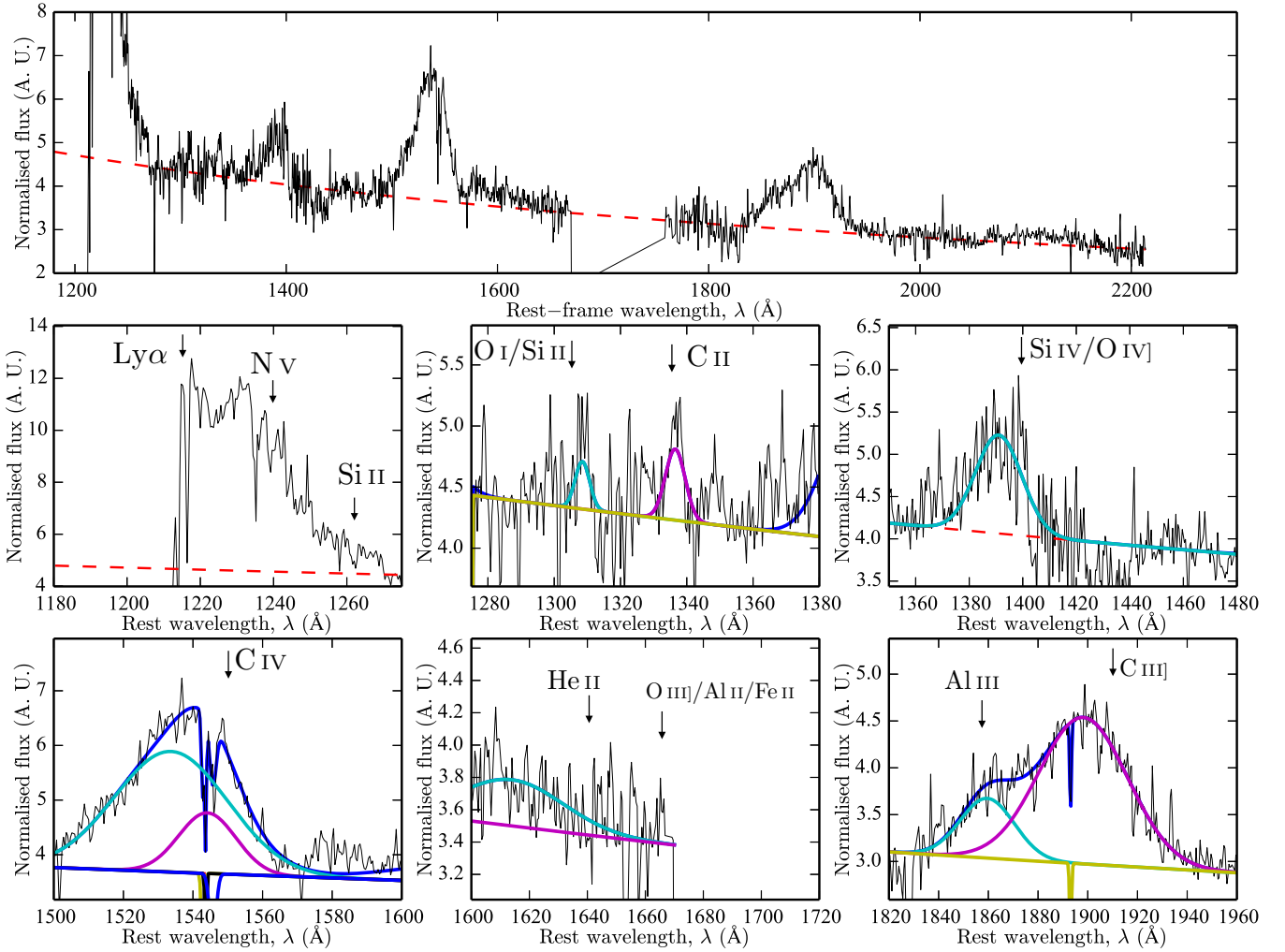


Figure 1. A zoom-in highlighting the MCMC QSO fitting procedure of Greig et al. (2016) applied to the rest-frame FIRE spectrum (Simcoe et al. 2012). This method includes the identification of ‘absorption’ features (e.g. the bottom-left and bottom-right panels), which improves our ability to recover the emission line profiles. The flux is normalized to unity at 1450 Å rest frame ($1 \text{ au} = 10^{-17} \text{ erg cm}^{-2} \text{ s}^{-1} \text{ Å}^{-1}$). Arrows denote the systemic redshift of each line, obtained from the recovered atomic [C II] redshift (Venemans et al. 2012). Top: a single power-law continuum component fit to the QSO spectrum (red dashed curve). Middle left: the obscured Ly α peak profile (not-fit). Middle centre: two low-ionization lines, O I/Si II] (cyan), and C II (magenta). Middle right: single-component Gaussian fit to the Si IV+O IV] blended line complex. Bottom left: two-component fit to C IV. Bottom centre: low-ionization lines, He II (cyan; no prevalent emission, therefore the line profile is unconstrained) and O III] (within the excised region, therefore not fit). Bottom right: single-component fit to C III] (magenta) and single Gaussian Al III component (cyan).

2.1.1 Reconstruction procedure

Within this section, we briefly summarize the major steps of the intrinsic Ly α profile reconstruction method of Greig et al. (2016), and refer the reader to that work for more in-depth discussions. Our approach is based on a covariance matrix characterizing the emission-line parameters. We first select a subsample of moderate- z ($2.08 < z < 2.5$), high S/N (> 15) QSOs from SDSS-III (BOSS) DR12 (Dawson et al. 2013; Alam et al. 2015). Each QSO in our final sample of 1673 (using the ‘Good’ sample, which provides tighter constraints on the reconstruction profile) is then fit with a single power-law continuum, and a set of Gaussian profiles to characterize the emission lines and any possible absorption features contaminating the observed QSO spectrum. Each Gaussian profile is described by three parameters: a line width, peak height, and velocity offset from the systemic redshift. For Ly α and C IV, we allow for both a broad and narrow component Gaussian to describe the line profile, and single components for all other high- and

low-ionization lines. After fitting all QSOs, and performing a visual quality assessment to refine our QSO sample, we construct our covariance matrix from the four most prominent high-ionization lines, Ly α , C IV, Si IV+O IV] and C III].

With the covariance matrix in hand, we can reconstruct the intrinsic Ly α line profile of ULASJ1120 as follows:

- (i) Using the fitting procedure described above, we fit the spectrum of ULASJ1120 far redward of the extent of the Ly α line profile. We chose $\lambda > 1275 \text{ Å}$ as the blue edge for the fit somewhat arbitrarily, but verify that this choice does not have an impact on the results.
- (ii) From this fit (shown in Fig. 1), we obtain estimates of ULASJ1120’s continuum and of its Si IV+O IV], C IV, and C III] line profiles.
- (iii) Using these estimates, we collapse the 18-dimensional (Gaussian-distributed) covariance matrix into a six-dimensional

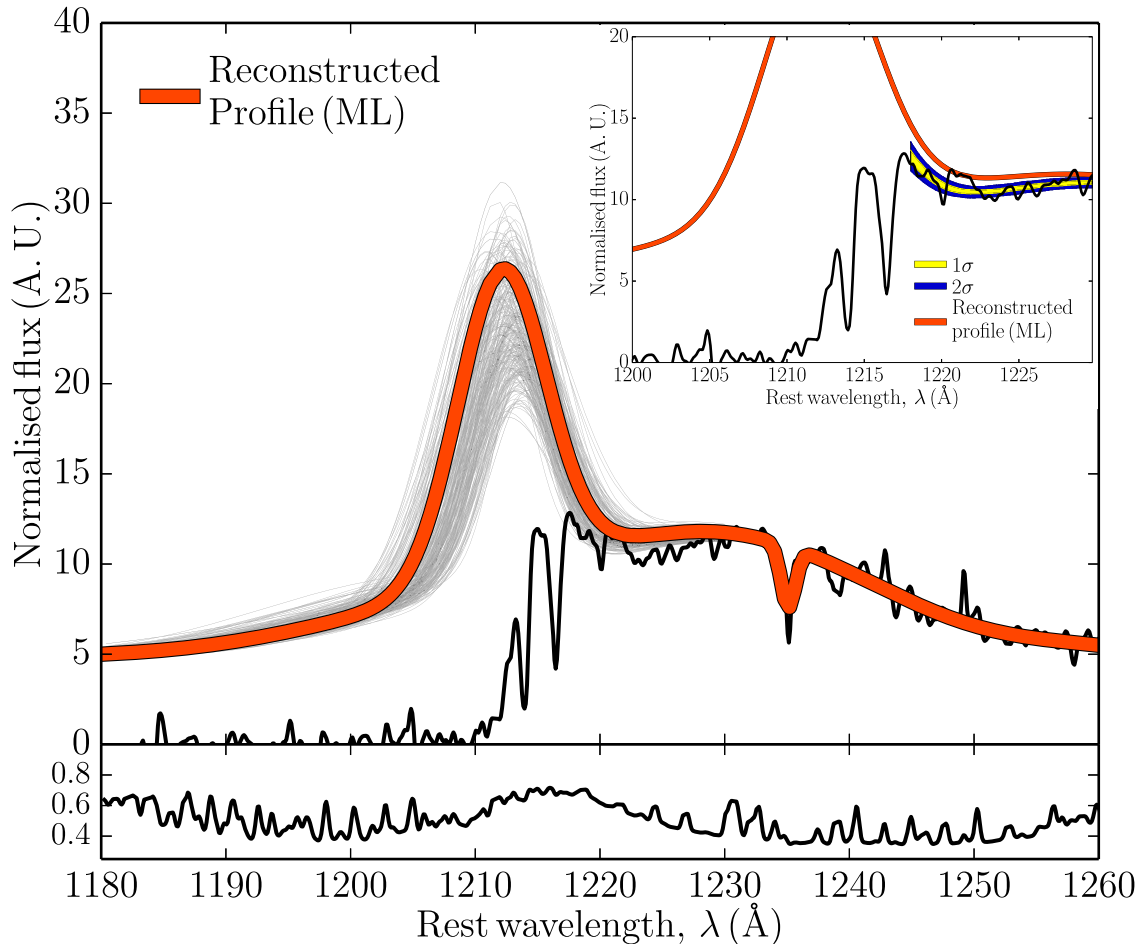


Figure 2. The reconstructed maximum likelihood $\text{Ly}\alpha$ emission line profile (red curve; shown for visualization purposes only) recovered from our covariance matrix method including an additional prior on the flux amplitude within the wavelength range $1230 < \lambda < 1275 \text{ \AA}$. The thin grey curves denote a subsample of 300 $\text{Ly}\alpha$ line profiles extracted from the reconstructed six-dimensional $\text{Ly}\alpha$ likelihood function (note, we sample 10^5 profiles in our full analysis). These curves are selected to be within 68 per cent of the maximum likelihood profile, and highlight the relative scale of the errors on the reconstructed $\text{Ly}\alpha$ line profile and fully encapsulate the intrinsic object-to-object variation of the QSO sample. The black curve denotes the observed spectrum of ULASJ1120, which has been resampled on to 0.1 \AA bins purely for the purposes of this figure (the full analysis pipeline uses the unaltered spectrum as shown in Fig. 1). Lower panel: the corresponding unaltered error spectrum of ULASJ1120 averaged on to 0.1 \AA bins. Inset: a zoom-in around $\text{Ly}\alpha$ highlighting the recovered imprint of the IGM damping wing profile (Section 2.3). The yellow (blue) shaded region denotes the 1σ (2σ) span of total (intrinsic + damping wing absorption) flux over the fitted region. For reference, the red curve is the maximum likelihood intrinsic profile (same as main figure). The stretch between 1222 and 1227 \AA is especially difficult to match without the aid of the IGM damping wing from an incomplete reionization.

estimate of the intrinsic $\text{Ly}\alpha$ emission line profile (two-component Gaussian each with an amplitude, width and velocity offset).

(iv) We apply a prior within the range $1230 < \lambda < 1275 \text{ \AA}$. This is performed by simultaneously fitting the $\text{Ly}\alpha + \text{N V}$ (1240.81 \AA) and Si II (1262.59 \AA) lines (where we sample the $\text{Ly}\alpha$ profile from the six-dimensional distribution), using the observed noise from the FIRE spectrum to obtain a χ^2 likelihood for the reconstructed profile. In other words, we require our profiles to fit the observed spectrum over the range $1230 < \lambda < 1275 \text{ \AA}$. This final step notably reduces the errors on the reconstructed $\text{Ly}\alpha$ profile (shown in Fig. 2), ruling out extreme profiles which are inconsistent with the actual observed spectrum. We note that the wavelength range by construction has to be redward of any significant damping wing absorption.

It is important to note that the actual range of the prior is not important for the reconstruction of the $\text{Ly}\alpha$ line profile (Greig et al. 2016). However, since we fit the IGM damping wing far redward of the line centre, out to 1230 \AA , it is critical that this prior range includes

sufficient information to allow for the fitting of the nearby N V line. While near the $\text{Ly}\alpha$ line centre, the total QSO flux is expected to be solely dominated by the $\text{Ly}\alpha$ line, further redward of the line centre one can expect an increasing contribution from the N V line as its line centre is approached. Unfortunately, simultaneously reconstructing the $\text{Ly}\alpha$ and N V emission lines would yield uncertainties, which are too large. Thus, we impose a prior just blueward of the N V line. As this lower limit is increased from our adopted 1230 \AA moving into the line, the spread in the allowed QSO flux will increase, broadening the recovered constraints on the IGM neutral fraction.

2.1.2 Reconstruction of ULASJ1120+0641

In Fig. 1, we present the MCMC template fitting of ULASJ1120 at $\lambda > 1275 \text{ \AA}$. In the top panel, the red-dashed curve corresponds to the best-fitting QSO continuum, whereas in the remaining zoomed-in

panels, we present the best-fits to the various emission line profiles, using either a single- or double-component Gaussian, as described above. Compared to the QSO spectra used in the construction of the covariance matrix in Greig et al. (2016), the FIRE spectrum is considerably noisier.

Immediately obvious from Fig. 1 is the significant blueshift observed amongst all the high-ionization lines. In addition to the already reported strong blueshift of C IV Mortlock et al. (2011), we note that the N V (not fit), Si IV+O IV] and C III] lines appear to be equally strongly blue shifted. At the same time, the low-ionization lines, O I and C II do not appear to be blue shifted at all. Furthermore, while not shown in Fig. 1 or observed in the Simcoe et al. (2012) FIRE spectrum, the Mg II line also does not have a significant blueshift (Mortlock et al. 2011). This behaviour is well known, which highlights that the physics governing the low- and high-ionization lines stems from different processes or physical regions. We stress that this strong observed blueshift in all high-ionization lines is automatically accounted for by the covariance matrix reconstruction pipeline.

Note that, in the FIRE spectrum, the Si IV+O IV] line is strongly affected by both night sky OH lines and telluric absorption bands. While attempts were made to correct this in the spectrum, they will still leave an imprint in the form of lower S/N and larger residuals. Within this work we attempt to mask out the worst of these lines; however, we caution that the Si IV+O IV] line may still be contaminated. However, we note that the Si IV+O IV] emission line is the least important of the three high-ionization lines used to reconstruct the intrinsic Ly α line profile. Therefore, while the characterization of the Si IV+O IV] line profile is likely to be contaminated, the uncertainties arising from this will not greatly impact our reconstructed Ly α line profile.

In Fig. 2, we show the reconstructed intrinsic Ly α emission line profile. The red curve is the best-fitting reconstructed profile (shown for visualization purposes only) obtained by jointly sampling the Ly α line profile and the wavelength range $1230 < \lambda < 1275 \text{ \AA}$, while the black curve is the observed spectrum sampled in 0.1 \AA bins.⁷ Given that our reconstruction procedure returns a six-dimensional likelihood function, in order to characterize the scale of the 68 per cent uncertainties on the reconstructed Ly α profile, we randomly sample this likelihood function to extract representative profiles. In Fig. 2, we present a subsample of 300 reconstructed Ly α line profiles denoted by the thin grey lines, which are within the 68 per cent uncertainties. These profiles highlight the relative scale of the variations in the total Ly α line profile peak height, width and location. Note, our analysis pipeline operates directly on a large number of these sampled profiles (drawn from the full distribution), and not the maximum-likelihood reconstructed profile (red curve).

Qualitatively, the reconstructed Ly α line profile is similar to the composite QSO spectrum presented in Mortlock et al. (2011) and in Simcoe et al. (2012), albeit with a slightly higher amplitude at the Ly α line centre. A notable advantage of our approach is the statistical characterization of the Ly α line offset, using the covariance matrix. As shown in Bosman & Becker (2015), the location of the Ly α line centre of the reconstructed profile is crucial for the analysis of the IGM damping wing. Unfortunately, the blueshifts observed in ULASJ1120 exceed those found in all of the 1673 QSOs from

which we construct the covariance matrix. The mean blueshift of the C IV ionization line profile of ULASJ1120 (obtained from combining the narrow and broad components), $\Delta v \sim 2500 \text{ km/s}$, is a $\sim 4\sigma$ outlier from our QSO sample. Thus in the reconstruction procedure for ULASJ1120, we have to extrapolate the Gaussian covariances.

We can test this extrapolation in two ways: (i) by testing our reconstruction approach against the most heavily blue-shifted QSOs within the sample used to construct the covariance matrix and (ii) by artificially removing the strong observed blueshift. In Appendix A, we explore the former, finding little evidence for a reduction in the quality of reconstructed Ly α profiles for the 50 most extreme objects in our sample.⁸ For the latter, we take the systemic redshift to be that from the C III] line (instead of our fiducial atomic [C II]). As noted in Section 2.1.2, the C III] emission line appears equally strongly blue shifted as C IV and the other high ionization lines; therefore, by using the C III] redshift, we can artificially remove the strong C IV velocity offset. After performing the Ly α reconstruction pipeline on this artificially corrected spectrum, we recover a quantitatively similar Ly α line profile shape, well within our 1σ uncertainties. Therefore, following these two tests, we can be relatively confident in the extrapolation of these Gaussian covariances to the values found in ULASJ1120.

2.2 The IGM damping wing during the EoR

As stated above, the observed spectrum redward of the Ly α line centre depends on the intrinsic emission (discussed in the previous section), and the damping wing absorption from (putative) cosmic H I patches along the line of sight (LoS). To statistically characterize the latter, we make use of the publicly available Evolution of 21-cm Structure (EOS; Mesinger et al. 2016)⁹ 2016 data release. These semi-numerical reionization simulations are 1.6 Gpc on a side with a 1024^3 grid and include state-of-the-art subgrid prescriptions for inhomogeneous recombinations and photo-heating suppression of star formation. The 2016 EOS data release corresponds to two simulation runs, with the efficiency of supernovae feedback adjusted to approximately bracket the expected EoR contribution from faint galaxies. The two runs are:

- (i) *Faint galaxies* – the EoR is driven by galaxies residing in haloes with masses of $10^8 \lesssim M_h/M_\odot \lesssim 10^9$, and is characterized by numerous small cosmic H II regions. Hereafter we will refer to the EoR morphologies resulting from this simulation as SMALL H II.
- (ii) *Bright galaxies* – the EoR is instead driven by galaxies residing in haloes with masses of $M_h \sim 10^{10} M_\odot$, and is characterized by spatially more extended H II structures. We refer to these simulated EoR morphologies as LARGE H II.

We note that the LARGE H II ionization fields have a factor of \sim few–10 times more power on large scales during the EoR, compared to the SMALL H II ionization fields. Although these are two opposite extremes in terms of H II region sizes, the SMALL H II EoR morphology is likely more realistic (see the discussion in Mesinger et al. 2016), and so we use this simulation as our fiducial model. Nevertheless, we include both extremes to explore the dependence of our results on EoR morphology.

⁷ Note, the choice to resample the spectrum is purely for visual representation. The original, unaltered spectrum (e.g. Fig. 1) is used within our full analysis pipeline.

⁸ Note that the C IV blueshifts for this sample of 50 QSOs were between 1300 and 2000 km s^{-1} , smaller than the recovered 2500 km s^{-1} of ULASJ1120 (see Fig. A1).

⁹ <http://homepage.sns.it/mesinger/EOS.html>

We construct samples of sightlines through our simulations which are terminated on one end at a halo, and then extended in a random direction through the simulation volume for a distance of 200 comoving Mpc. Along each sightline, we sum the contributions from all encountered H I patches to construct a composite optical depth for the damping wing (e.g. Miralda-Escudé 1998). We purposefully exclude the H I contribution from pixels ≤ 16 comoving Mpc (2 physical Mpc) from the QSO host halo. This corresponds to the minimum possible radius of the H II region around ULASJ1120 inferred from measurements of its near zone (Mortlock et al. 2011). We do not explicitly include the flux from the QSO in our reionization maps. Doing so would require assumptions about the QSO lifetime and ionizing luminosity. Neglecting the QSO ionizing contribution implies that the surrounding H II region could be larger than predicted by our EoR models. For a given \bar{x}_{HII} a larger surrounding H II region implies a smaller integrated damping wing optical depth. Thus if the QSO contributes in growing the surrounding H II region, our modelled optical depths should be associated with even higher values of \bar{x}_{HII} , shifting the probability distribution functions (PDFs) we present below towards larger \bar{x}_{HII} .

At $z = 7.1$, we select 10^4 identified haloes in the mass range $6 \times 10^{11} < M_{\text{h}}/M_{\odot} < 3 \times 10^{12}$, consistent with the inferred dynamical mass of the host halo of ULASJ1120 (Venemans et al. 2012). Importantly, these higher host halo masses, made possible by the large-scale EOS simulations, are a notable improvement over previous studies (e.g. Bolton et al. 2011) as they better capture the bias and scatter of the QSOs locations inside reionization fields. Though the lines of sight begin 16 Mpc from the host haloes, this bias and scatter may still be important (see e.g. fig. 2 of Mesinger & Furlanetto 2008 and fig. 3 of Mesinger 2010). We use 10 LoSs per host halo, resulting in a total sample of 10^5 synthetic IGM damping wing profiles for each sampled \bar{x}_{HII} and EoR morphology (SMALL H II and LARGE H II). Since we wish to leave the IGM neutral fraction at $z = 7.1$ as a free parameter, we follow the common practice of sampling ionization fields at various redshifts corresponding to a given \bar{x}_{HII} . That is, we use the same halo list obtained from the $z = 7.1$ snapshot to define the locations for our synthetic damping wing profiles, but vary the mean IGM neutral fraction by sampling the corresponding ionization fields obtained from different redshift outputs. Such an approach is justified as the ionization fields are largely redshift independent, when compared at a fixed \bar{x}_{HII} (e.g. McQuinn et al. 2007a,b; Sobacchi & Mesinger 2015).

2.3 Joint fitting of the intrinsic emission and IGM damping wing

Having outlined the reconstruction of the intrinsic Ly α line profile of ULASJ1120 in Section 2.1 and the IGM damping wing profiles in Section 2.2, we now combine them to simultaneously fit the observed spectrum. Our fitting procedure consists of the following steps:

- (i) The intrinsic Ly α line profile recovered in Section 2.1.2 is fully described by a six-dimensional likelihood function (three parameters for each of the two Gaussian components), characterizing the uncertainties and correlations amongst the Ly α line profile parameters, constrained by the spectrum at $\lambda > 1230$ Å. We draw $\sim 10^5$ Ly α line profiles directly from this six-dimensional likelihood.
- (ii) Each line profile is then multiplied by each of the 10^5 EoR damping wing absorption profiles, resulting in a total sample of $\sim 10^5 \times 10^5$ mock spectra for each value of \bar{x}_{HII} .

- (iii) Each mock spectrum is then compared with the observed spectrum of ULASJ1120 in the wavelength range $1218 \text{ Å} < \lambda < 1230 \text{ Å}$.¹⁰ The quality of the fit is characterized by a (χ^2 based) likelihood, using the observational errors of the spectrum.

- (iv) The resulting likelihood, averaged over all $\sim 10^{10}$ mock spectra, is then assigned to that particular \bar{x}_{HII} .

- (v) Steps (ii)–(iv) are repeated for each trial value of \bar{x}_{HII} . We sample the range $0.01 \leq \bar{x}_{\text{HII}} \leq 0.95$, with 40 (28) individual snapshots for the SMALL H II (LARGE H II) simulations (note that the EoR proceeds more rapidly in the LARGE H II model, resulting in a coarser \bar{x}_{HII} sampling for outputs at fixed redshift intervals).

- (vi) We normalize the resulting relative likelihoods, ending with a final 1D PDF of \bar{x}_{HII} for each of the EoR morphologies.

The above steps effectively result in the construction of a 3D likelihood which is a function of: (i) \bar{x}_{HII} ; (ii) the EoR damping wing sightline; and (iii) the intrinsic emission profile. Our final constraints on \bar{x}_{HII} are obtained by marginalizing over (ii) and (iii).

3 RESULTS

In the inset of Fig. 2, we present the confidence intervals on the product of the reconstructed Ly α line profile and the synthetic IGM damping wing profiles within the fitting interval $1218 \text{ Å} < \lambda < 1230 \text{ Å}$. For reference, the red curve is the intrinsic Ly α emission line profile with the maximum likelihood from our reconstruction procedure. The impact of the damping wing contribution is highlighted by the offset of the shaded regions and the red curve. In the main panel of Fig. 2, we present a small subset (300) of recovered Ly α line profiles to convey the relative uncertainties in the reconstruction pipeline. Note that the wavelength stretch between 1222 and 1227 Å is especially difficult to fit purely with the intrinsic profiles alone. As we shall see below, we require a non-zero IGM damping wing contribution to fit the observed spectrum of ULASJ1120.

Before presenting our final constraints on \bar{x}_{HII} , we showcase the EoR sightline-to-sightline scatter in Fig. 3. For each of the randomly selected subsamples of 1000 sightlines shown in the figure, we average over the full distribution of the reconstructed Ly α intrinsic profiles, in order to generate a \bar{x}_{HII} PDF for that sightline. Collapsing (marginalizing) over the vertical direction (sightline number) for the entire sample of 10^5 LoSs recovers the full 1D marginalized PDF [step (vi) of Section 2.3; see Fig. 4]. Sightlines extracted from the SMALL H II and LARGE H II simulations appear on the left and right, respectively.

On average, we recover a similar range for the preferred IGM neutral fraction for both EoR morphologies. However, there is significant sightline-to-sightline variation, shifting the peaks of the \bar{x}_{HII} distributions by tens of per cent. This highlights the importance of sampling a large number of IGM damping wing profiles. Our full sample consists of 10^5 sightlines through inhomogeneous

¹⁰ The choice of 1230 Å is motivated by the blue edge of the prior discussed in Section 2.1.2, while the choice of 1218 Å is motivated by ensuring that we are sufficiently far from the influence of any infalling or local gas (e.g. Barkana & Loeb 2004), which is not modelled by our EoR simulations. Note that the circular velocity of the host halo (e.g. Venemans et al. 2012) corresponds to a rest-frame offset of ~ 2 Å. We verify that changing this range only impacts our \bar{x}_{HII} constraints at the per cent level by considering the following alternatives: $1220 \text{ Å} < \lambda < 1230 \text{ Å}$, $1220 \text{ Å} < \lambda < 1228 \text{ Å}$, and $1218 \text{ Å} < \lambda < 1228 \text{ Å}$.

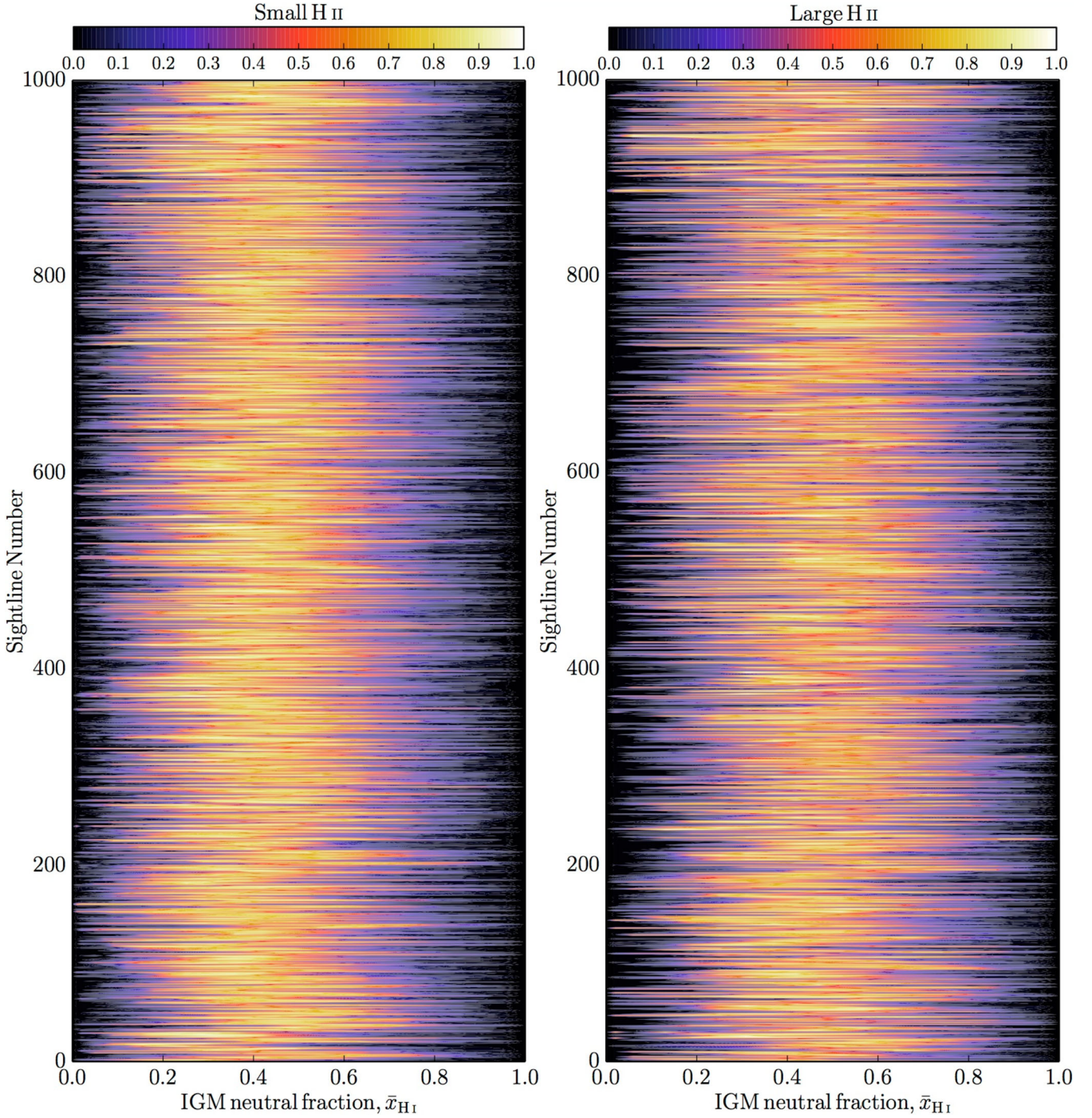


Figure 3. 1D PDFs of the IGM neutral fraction drawn from a subsample of 1000 lines of sight for each of the two EoR simulations used in our analysis (Mesinger et al. 2016). Colour bars denote the amplitude of the PDFs, $P(\bar{x}_{\text{H I}})$. Note that the peaks of the PDFs of each sightline are normalized to unity purely to aid the visualization. The shifting locations of the peaks per sightline are indicative of the sightline-to-sightline variation. In the left-hand panel, the individual sightline PDFs correspond to the SMALL H II EoR simulations (reionization driven by faint galaxies producing small cosmic H II regions) whereas the right-hand panel corresponds to the LARGE H II EoR simulations (reionization driven by bright galaxies producing large cosmic H II regions). Averaging over the full sample of 10^5 sightlines (i.e. collapsing along the vertical direction) results in the 1D PDFs of $\bar{x}_{\text{H I}}$ shown in the following figure.

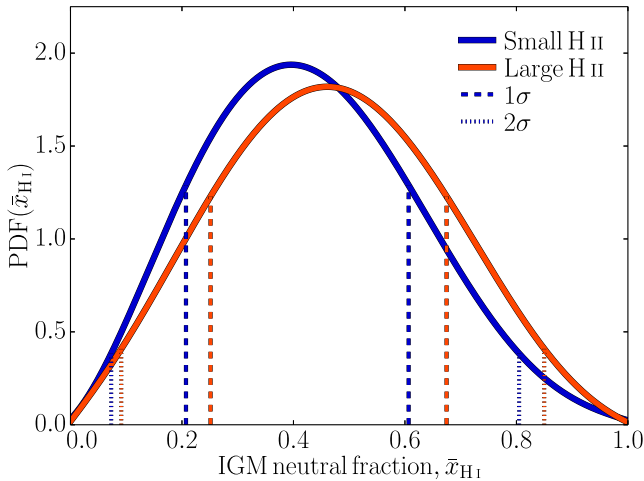


Figure 4. PDFs of the $z = 7.1$ IGM neutral fraction obtained by marginalizing over all synthetic IGM damping wing absorption profiles and reconstructed intrinsic Ly α emission line profiles. The red curve corresponds to the LARGE H II simulations (right-hand panel of Fig. 3) whereas the blue curve corresponds to the SMALL H II simulation (left-hand panel of Fig. 3). Dashed (dotted) curves correspond to the 1σ (2σ) constraints on \bar{x}_{HI} for the respective morphologies. Both simulations recover consistent results, favouring a strong damping wing imprint from a significantly neutral IGM ($\bar{x}_{\text{HI}} \sim 0.4$).

reionization, compared with 100 sightlines through homogeneous reionization in the preliminary studies of Bolton et al. (2011) and Keating et al. (2015).

Finally, in Fig. 4 we present the main result of this work: 1D PDFs of \bar{x}_{HI} .¹¹ These are obtained by marginalizing over all combinations of reconstructed intrinsic Ly α line profiles and synthetic IGM damping wing sightlines for a given \bar{x}_{HI} . The blue curve corresponds to the SMALL H II EoR morphology, while the red curve corresponds to the LARGE H II EoR morphology. Dotted (dashed) curves correspond to the 1 (2σ) constraints on \bar{x}_{HI} for the respective morphologies:

- (i) SMALL H II; $\bar{x}_{\text{HI}} = 0.40^{+0.21}_{-0.19}$ (1σ) and $0.40^{+0.41}_{-0.32}$ (2σ)
- (ii) LARGE H II; $\bar{x}_{\text{HI}} = 0.46^{+0.21}_{-0.21}$ (1σ) and $0.46^{+0.39}_{-0.37}$ (2σ).

As mentioned earlier (and discussed in Mesinger et al. 2016), the SMALL H II model is likely more accurate and we adopt it as our fiducial constraint. We note that the constraints on \bar{x}_{HI} are very similar for both SMALL H II and LARGE H II. This indicates that the damping wing imprint is not very sensitive to how the cosmic neutral patches are distributed at a fixed value of \bar{x}_{HI} .

From the recovered PDF of the IGM neutral fraction, we can strongly infer the presence of a damping wing signature, with no IGM damping wing contribution being inconsistent at $>2\sigma$. This is despite the fact that at first glance in Fig. 2, the reconstructed Ly α profiles (without damping wing absorption) appear to be consistent with the observed spectrum of ULASJ1120 in the lower end of the 1218–1221 Å wavelength range used in our analysis. In Appendix C, we quantify this in detail by performing our full analysis pipeline on smaller, equally spaced 3 Å subregions. The recovered constraints from the subregions are consistent with each other at 1σ , with the

strongest evidence for a damping wing coming from the 1222 to 1227 Å region of the observed spectrum.

How do these constraints tie into the existing picture of reionization? The best available, model independent constraints on the end stages of reionization are obtained from the dark fraction of pixels in the QSO spectra (McGreer, Mesinger & D’Odorico 2015), which imply the IGM neutral fraction to be $\bar{x}_{\text{HI}} \lesssim 0.11$ (1σ). Therefore the $\bar{x}_{\text{HI}} = 0.40^{+0.21}_{-0.19}$ constraints obtained here imply an evolution of $\Delta\bar{x}_{\text{HI}} \sim 0.1$ – 0.5 over the redshift interval $z \approx 7 \rightarrow 6$. This is consistent with the currently available EoR constraints (see Greig & Mesinger 2017 and references therein).

4 COULD THE DAMPING WING COME FROM A DAMPED LYMAN ALPHA SYSTEM?

In this work, we found evidence of a damping wing imprint on the red side of the Ly α line of ULASJ1120 and quantified the corresponding constraints on the IGM neutral fraction. However, a damping wing could instead be produced by an intervening damped Ly α system, at least in principle. Indeed most high- z gamma-ray bursts (GRBs) show evidence of a DLA in their spectra (e.g. Chornock et al. 2013, 2014; Totani et al. 2014). However, the GRB DLAs are associated with the GRB host galaxy, while a DLA in the spectra of ULASJ1120 would have to be at least 16 Mpc away from the QSO host galaxy. As has been pointed out previously, finding such an object in a random skewer through the IGM is highly unlikely. To mimic our results, the required column density of the DLA would have to be $\log_{10}(N_{\text{HI}}/\text{cm}^{-2}) > 20 - 21$ (see also Simcoe et al. 2012; Schroeder et al. 2013). Such systems are extremely rare. Following Schroeder et al. (2013), we note that an extrapolation of the incidence rate of DLAs (Prochaska & Wolfe 2009; Songaila & Cowie 2010) to $z \sim 7$ implies an abundance of $\lesssim 0.05$ DLAs per unit redshift with comparable column densities (see fig. 8 in Songaila & Cowie 2010). Thus only $\lesssim 0.3$ per cent of IGM segments with a length corresponding to the ULASJ1120 near zone size ($\Delta z_{\text{NZ}} \sim 0.05$) would contain a DLA. We also note that Bolton et al. (2011) found only ~ 5 per cent of their mock sightlines contained a DLA, even using a self-shielding prescription which notably overestimates their abundances (Rahmati et al. 2013; Keating et al. 2014; Mesinger et al. 2015). Thus, the a priori presence of a DLA can approximately be excluded at $\lesssim 2\sigma$ to 3σ on the basis of the required column density alone.

Even more damning is the fact that there is no evidence of associated metal line absorption in ULASJ1120. Therefore, a putative DLA would have to be atypically pristine, with a metallicity of $Z \lesssim 10^{-4} Z_{\odot}$ which is inconsistent with every other DLA observation (e.g. Simcoe et al. 2012; Cooke, Pettini & Jorgenson 2015). We therefore conclude that the damping wing absorption seen in ULASJ1120 is highly unlikely to originate from a DLA.

5 CONCLUSION

In this work, we obtain constraints on the $z = 7.1$ IGM neutral fraction by isolating its damping wing absorption in the spectrum of QSO ULASJ1120. We use a state-of-the-art Bayesian framework which for the first time is able to jointly sample both: (i) the uncertainty in the QSO intrinsic emission; and (ii) the EoR sightline-to-sightline variation. For (i), we use a covariance matrix of emission line properties (Greig et al. 2016) to reconstruct the intrinsic Ly α line profile. For (ii), we use the latest, large-scale simulations of patchy reionization (Mesinger et al. 2016). After marginalizing over (i) and (ii), we obtain robust constraints on the IGM neutral fraction. For our fiducial reionization model, these

¹¹ In Appendix B, we explore the impact of potential errors in the flux calibration of ULASJ1120, and how this could impact the overall constraints on the IGM neutral fraction. By including a conservative 10 per cent error on the QSO continuum we find, for the SMALL H II model, constraints consistent with the main results of this paper.

are: $\bar{x}_{\text{H I}} = 0.40^{+0.21}_{-0.19}$ (1σ) and $0.40^{+0.41}_{-0.32}$ (2σ). We note that the constraints are very insensitive to the EoR model, at a fixed global neutral fraction (see Fig. 4).

Our results correspond to the first measurement of the ionization state of the IGM at $z \sim 7$, with a well-defined confidence range (as opposed to upper/lower limits). They are consistent with the latest *Planck* measurements of the Thompson scattering optical depth, which independently appeared as this work was nearing completion (Planck Collaboration XLVII 2016).

The framework we developed can easily be applied to future QSO observations. Moreover, the analysis can be extended to incorporate the transmission statistics in the QSO near zone (blueward of $\text{Ly}\alpha$). This would introduce additional uncertainties, but would allow the analysis to be extended to other bright $z \sim 6\text{--}7$ QSOs which have a much larger near zone, and thus a correspondingly weaker damping wing imprint on the red side of the line (Schroeder et al. 2013). We defer this to future work.

ACKNOWLEDGEMENTS

We thank Ian McGreer for providing helpful comments on a draft version of this manuscript. Additionally, we thank the anonymous referee for their detailed and helpful suggestions which have improved the quality of this work. AM and BG acknowledge funding support from the European Research Council (ERC) under the European Union's Horizon 2020 research and innovation programme (grant agreement No. 638809 – AIDA – PI: AM). ZH is supported by NASA grant NNX15AB19G. RS is supported by NSF grant AST-1109915.

REFERENCES

- Alam S. et al., 2015, *ApJS*, 219, 12
 Barkana R., Loeb A., 2004, *ApJ*, 601, 64
 Bolton J. S., Haehnelt M. G., 2007a, *MNRAS*, 381, L35
 Bolton J. S., Haehnelt M. G., 2007b, *MNRAS*, 374, 493
 Bolton J. S., Haehnelt M. G., Warren S. J., Hewett P. C., Mortlock D. J., Venemans B. P., McMahon R. G., Simpson C., 2011, *MNRAS*, 416, L70
 Boroson T. A., Green R. F., 1992, *ApJS*, 80, 109
 Bosman S. E. I., Becker G. D., 2015, *MNRAS*, 452, 1105
 Carilli C. L. et al., 2010, *ApJ*, 714, 834
 Caruana J., Bunker A. J., Wilkins S. M., Stanway E. R., Lorenzoni S., Jarvis M. J., Ebert H., 2014, *MNRAS*, 442, 2831
 Chornock R., Berger E., Fox D. B., Lunnan R., Drout M. R., Fong W., Laskar T., Roth K. C., 2013, *ApJ*, 774, 26
 Chornock R., Berger E., Fox D. B., Fong W., Laskar T., Roth K. C., 2014, preprint (arXiv:1405.7400)
 Cooke R. J., Pettini M., Jorgenson R. A., 2015, *ApJ*, 800, 12
 Dawson K. S. et al., 2013, *AJ*, 145, 10
 Fan X. et al., 2006, *AJ*, 132, 117
 Francis P. J., Hewett P. C., Foltz C. B., Chaffee F. H., 1992, *ApJ*, 398, 476
 George E. M. et al., 2015, *ApJ*, 799, 177
 Greig B., Mesinger A., 2017, *MNRAS*, 465, 4838
 Greig B., Mesinger A., McGreer I. D., Gallerani S., Haiman Z., 2016, preprint (arXiv:1605.09388)
 Haiman Z., Spaans M., 1999, *ApJ*, 518, 138
 Keating L. C., Haehnelt M. G., Becker G. D., Bolton J. S., 2014, *MNRAS*, 438, 1820
 Keating L. C., Haehnelt M. G., Cantalupo S., Puchwein E., 2015, *MNRAS*, 454, 681
 Kramer R. H., Haiman Z., 2009, *MNRAS*, 400, 1493
 Lee K.-G., Spergel D. N., 2011, *ApJ*, 734, 21
 Maio U., Ciardi B., Müller V., 2013, *MNRAS*, 435, 1443
 Maselli A., Gallerani S., Ferrara A., Choudhury T. R., 2007, *MNRAS*, 376, L34
 McGreer I. D., Mesinger A., D'Odorico V., 2015, *MNRAS*, 447, 499

- McQuinn M., Hernquist L., Zaldarriaga M., Dutta S., 2007a, *MNRAS*, 381, 75
 McQuinn M., Lidz A., Zahn O., Dutta S., Hernquist L., Zaldarriaga M., 2007b, *MNRAS*, 377, 1043
 Mesinger A., 2010, *MNRAS*, 407, 1328
 Mesinger A., ed. 2016, *Astrophysics and Space Science Library*, Understanding the Epoch of Cosmic Reionization: Challenges and Progress. Springer-Verlag, Berlin
 Mesinger A., Furlanetto S. R., 2008, *MNRAS*, 385, 1348
 Mesinger A., Haiman Z., Cen R., 2004, *ApJ*, 613, 23
 Mesinger A., Aykatalp A., Vanzella E., Pentericci L., Ferrara A., Dijkstra M., 2015, *MNRAS*, 446, 566
 Mesinger A., Greig B., Sobacchi E., 2016, *MNRAS*, 459, 2342
 Miralda-Escudé J., 1998, *ApJ*, 501, 15
 Mortlock D. J. et al., 2011, *Nature*, 474, 616 (ULASJ1120)
 Ono Y. et al., 2012, *ApJ*, 744, 83
 Ouchi M. et al., 2010, *ApJ*, 723, 869
 Pâris I. et al., 2011, *A&A*, 530, A50
 Pentericci L., 2011, *ApJ*, 443, 132
 Planck Collaboration XIII, 2016, *A&A*, 594, 13
 Planck Collaboration XLVII, 2016, *A&A*, 596, 19
 Prochaska J. X., Wolfe A. M., 2009, *ApJ*, 696, 1543
 Rahmati A., Pawlik A. H., Raičević M., Schaye J., 2013, *MNRAS*, 430, 2427
 Schenker M. A., Ellis R. S., Konidaris N. P., Stark D. P., 2014, *ApJ*, 795, 20
 Schroeder J., Mesinger A., Haiman Z., 2013, *MNRAS*, 428, 3058
 Simcoe R. A. et al., 2008, in *Proc. SPIE Conf. Ser. Vol. 7014*, Ground-based and Airborne Instrumentation for Astronomy II SPIE, Bellingham, p. 27
 Simcoe R. A., Sullivan P. W., Cooksey K. L., Kao M. M., Matejek M. S., Burgasser A. J., 2012, *Nature*, 492, 79
 Sobacchi E., Mesinger A., 2015, *MNRAS*, 453, 1843
 Songaila A., Cowie L. L., 2010, *ApJ*, 721, 1448
 Stark D. P., Ellis R. S., Chiu K., Ouchi M., Bunker A., 2010, *MNRAS*, 408, 1628
 Suzuki N., 2006, *ApJS*, 163, 110
 Suzuki N., Tytler D., Kirkman D., O'Meara J. M., Lubin D., 2005, *ApJ*, 618, 592
 Totani T. et al., 2014, *PASJ*, 66, 63
 Venemans B. P. et al., 2012, *ApJ*, 751, L25

APPENDIX A: EXTRAPOLATING OUR MODEL TO ULASJ1120

In this section, we explore the validity of extrapolating the Gaussian covariances between various line profile parameters recovered from Greig et al. (2016) in order to perform the $\text{Ly}\alpha$ profile reconstruction of ULASJ1120. The necessity of performing this extrapolation arises due to ULASJ1120's extremely large C IV blueshift, which is larger than any of the 1673 'good' QSOs originally considered for the construction of the covariance matrix in Greig et al. (2016). Owing to the rarity of these extremely blue-shifted sources, rather than searching for a sufficient statistical sample of similar sources in the BOSS data base, instead we investigate a subsample of the 50 most blue-shifted QSOs within our existing QSO sample.

In Fig. A1, we present the recovered C IV velocity offset of the narrow-line component (double-Gaussian line profile) against the ratio of the reconstructed QSO flux compared to the original QSO flux at 1220 Å. In Greig et al. (2016), we use this ratio as a metric to define how well the reconstruction pipeline performs. In this work, we distinguished a good characterization of the reconstructed $\text{Ly}\alpha$ profile being when this ratio was within 15 per cent¹² of the original fit to the QSO flux. As such, the horizontal red dashed line in Fig. C1 denotes this 15 per cent limit. The vertical red dashed

¹² This choice of 15 per cent was an arbitrary definition.

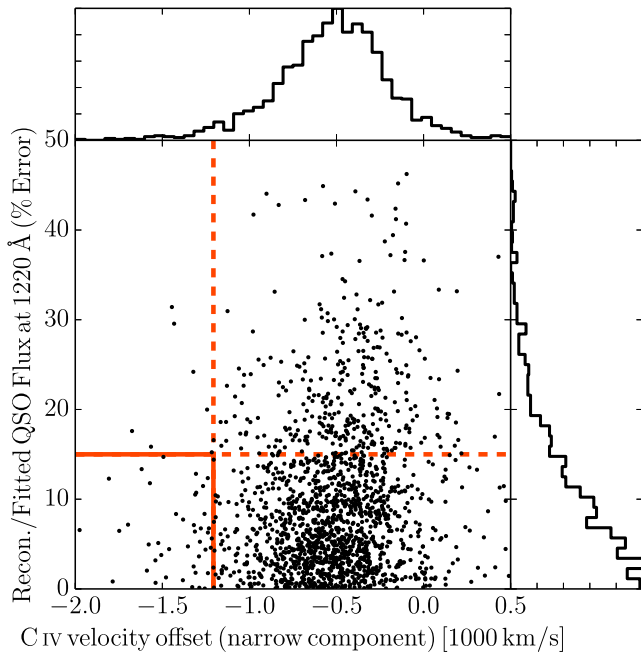


Figure A1. The C IV narrow component velocity offset against the percentage error on the reconstructed QSO flux compared to the original fit QSO flux at 1220 Å for the 1673 QSOs within the ‘good’ sample at $2.1 \lesssim z \lesssim 2.5$ (Greig et al. 2016). The vertical red dashed line denotes the 50 most heavily blue shifted QSOs (leftward of the line), while the red horizontal dashed line corresponds to a 15 per cent error in the reconstructed QSO flux compared to the original QSO flux. The solid red box highlights which of the 50 QSOs with the largest blueshift have reconstructed Ly α profiles within 15 per cent of the original QSO flux.

line corresponds to the smallest C IV velocity offset of the 50 most blue-shifted QSOs. The solid red box encompasses the QSOs which match both these criteria.

For the total sample of 1673 QSOs, at 1220 Å, Greig et al. (2016) found that the QSO flux could be recovered to within 15 per cent for 90 per cent of all QSOs. Applying this same criteria to the 50 most blue-shifted QSOs, we recover the QSO flux to within 15 per cent for 88 per cent of this sample. By recovering similar fractions for the 50 most blue-shifted QSOs compared to the full sample (88 compared with 90 per cent), it is clear that there is no obvious decrease in performance of the reconstruction procedure with increasingly larger C IV blueshifts. Furthermore, Fig. A1 shows no correlation between the quality of reconstruction and the C IV velocity offset. Finally, four of the five most extremely blue-shifted QSOs in our sample are recovered to less than 10 per cent of the original QSO flux at 1220 Å. Therefore, given that this reconstruction procedure performs equally well irrespective of the C IV blueshift, we find that it is reasonable to extrapolate the covariance matrix to the extreme C IV blueshift of ULASJ1120.

APPENDIX B: IMPACT OF CONTINUUM ERRORS OWING TO INCORRECT FLUX CALIBRATION

In this work, our observed spectrum of ULASJ1120 was obtained from the FIRE infrared spectrometer on the Magellan/Baade telescope. This data was measured using a narrow slit echelle spectrum, which are difficult to accurately flux calibrate. In this section, we

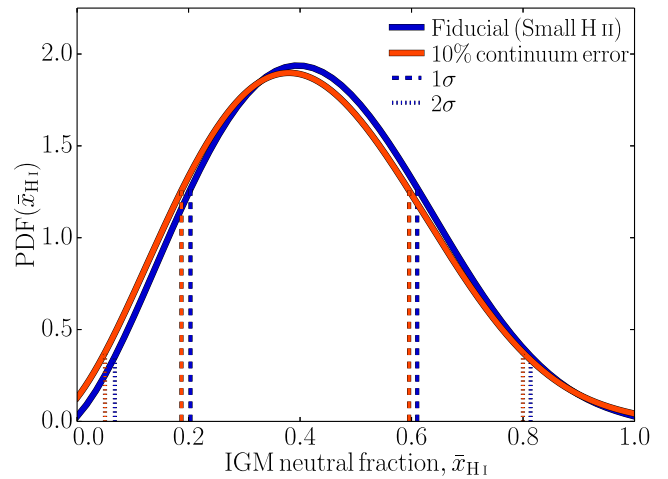


Figure B1. PDFs of the $z = 7.1$ IGM neutral fraction from the SMALL H II simulation including an additional uncertainty to mimic potential flux calibration errors. The blue curve corresponds to our fiducial PDF (blue curve in Fig. 4) while the red curve has an additional 10 per cent error added to the QSO continuum which is folded into our full analysis pipeline. Dashed and dotted curves correspond to the 1σ and 2σ constraints on the IGM neutral fraction.

explore what impact any potential flux calibration errors may have had on our inferred constraints on the IGM neutral fraction.

For this, we consider a constant 10 per cent error on the fitted QSO continuum power law from ULASJ1120 (obtained from our >1275 Å fit) over the full 1218–1230 Å damping wing fitting region. Note that in our reconstruction procedure it is non-trivial to include a direct uncertainty on the total flux amplitude. However, within this fitting region, the amplitude of the continuum constitutes ~ 50 per cent of the total flux; therefore, a 10 per cent error on the continuum roughly equates to an error on the total flux amplitude of ~ 5 per cent. We then repeat our full analysis pipeline outlined in Section 3 fitting for the IGM damping wing imprint, adding in this 10 per cent error in quadrature. In Fig. B1, we present the 1D PDFs of the IGM neutral fraction of the SMALL H II synthetic damping wing profiles. The blue curve corresponds to our fiducial constraints on the IGM neutral fraction (Fig. 4) whereas the red curve highlights the impact of the 10 per cent error on the QSO continuum, mimicking a flux calibration error.

From Fig. B1, it is evident that the inclusion of this additional source of error on the QSO continuum has very minimal impact on our constraints on the IGM neutral fraction. By including this error, we recover an IGM neutral fraction of $\bar{x}_{\text{H I}} = 0.38^{+0.22}_{-0.19}$ (1σ). This is essentially equivalent to our fiducial constraints of $\bar{x}_{\text{H I}} = 0.40^{+0.21}_{-0.19}$ (1σ), highlighting that our results are much more sensitive to the Ly α line recovery and the associated uncertainties, than the continuum.

This marginal reduction in the IGM neutral fraction arises from effectively broadening the distribution of reconstructed Ly α profiles which are capable of matching the observed spectrum (i.e. lowering the QSO continuum level of the reconstructed profiles, requiring smaller IGM neutral fractions to match ULASJ1120). This effect is most evident by the rising amplitude in the tail of the PDF near $\bar{x}_{\text{H I}} = 0$. Furthermore, as one would anticipate, by broadening the total errors applied to the recovery of the damping wing profile, the PDF of the IGM neutral fraction including this 10 per cent error, is marginally broader than the fiducial neutral fraction distribution. Importantly, given the very minor differences, we can confidently

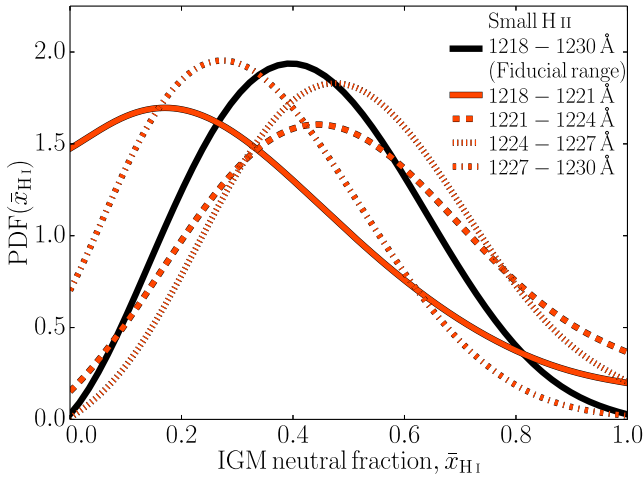


Figure C1. PDFs of the $z = 7.1$ IGM neutral fraction obtained by marginalizing over all synthetic IGM damping wing absorption profiles from the SMALL H II simulation and reconstructed intrinsic $\text{Ly}\alpha$ emission line profiles for various selected fitting intervals. The solid black curve corresponds to our full fiducial fitting interval, 1218–1230 Å (blue curve in Fig. 4). The red solid, dashed, dotted and dot-dashed curves correspond to four separate 3 Å fitting intervals: 1218–1221, 1221–1224, 1224–1227 and 1227–1230 Å, respectively.

conclude that our IGM neutral fraction constraints are not strongly impacted by any potential errors arising from problems in the flux calibration of FIRE spectrum of ULASJ1120.

APPENDIX C: EXPLORING VARIOUS FITTING RANGES

In Section 3, we presented our constraints on the IGM neutral fraction by fitting for a damping wing signature between 1218 and 1230 Å in the observed spectrum of ULASJ1120. In this section, we quantify how the different subregions within this wavelength range impact the final result. To test this, we break our fiducial fitting range into four 3 Å chunks and recover the inferred IGM neutral fraction for each 3 Å region independently.

In Fig. C1, we present the 1D PDFs of the IGM neutral fraction at $z = 7.1$ recovered from the SMALL H II simulation, for the various 3 Å intervals. The black curves correspond to our fiducial

Table C1. Tabulated values of the recovered IGM neutral fraction at $z = 7.1$ for the SMALL H II simulations when considering four smaller, equally spaced 3 Å regions within our fiducial fitting range of 1218–1230 Å.

Fitting region (SMALL H II)	$\bar{x}_{\text{HI}}(1\sigma)$	$\bar{x}_{\text{HI}}(2\sigma)$
1218–1230 Å (fiducial)	$0.40^{+0.21}_{-0.19}$	$0.40^{+0.41}_{-0.32}$
1218–1221 Å	$0.17 (\leq 0.44)$	$0.17 (\leq 0.82)$
1221–1224 Å	$0.44^{+0.27}_{-0.22}$	$0.44^{+0.50}_{-0.36}$
1224–1227 Å	$0.47^{+0.23}_{-0.20}$	$0.47^{+0.42}_{-0.35}$
1227–1230 Å	$0.28^{+0.21}_{-0.19}$	$0.28 (\leq 0.70)$

1218–1230 Å fitting interval, whereas the red solid, dashed, dotted, and dot-dashed curves correspond to the 1218–1221, 1221–1224, 1224–1227 and 1227–1230 Å sub-ranges, respectively. In Table C1, we summarize the recovered IGM neutral fractions and associated 1σ and 2σ errors for each of the fitting intervals considered.

Importantly, in each 3 Å interval there is always a clear preference for a damping wing imprint, implying we have not artificially biased our results by selecting a specific wavelength range to a priori require a damping wing signature. Even in the 1218–1221 Å region, where from Fig. 2 one might anticipate we would not require a strong damping wing signature (reconstructed $\text{Ly}\alpha$ profiles appear to pass through the observed spectrum), the highest likelihood is from an IGM neutral fraction of $\bar{x}_{\text{HI}} \sim 0.17$, although a fully ionized universe is consistent at 1σ . This interval however returns the largest uncertainties on the IGM neutral fraction. This is purely driven by the breadth in allowed QSO fluxes from the reconstructed $\text{Ly}\alpha$ profiles, due to the fact that this region is furthest from the edge of the applied prior in the reconstruction process (1230 Å).

In contrast, the 1222–1227 Å region of ULASJ1120 is particularly difficult to fit without requiring higher IGM neutral fractions. This behaviour is quantified by the two adjacent 3 Å intervals, 1221–1224 Å and 1224–1227 Å. Here, larger IGM neutral fractions of $\bar{x}_{\text{HI}} = 0.44$ and 0.47 are preferred.

Finally, we note that all of the sub-regions are consistent with one another at 1σ . Thus, there is no obviously spurious spectral feature biasing our fiducial results in one direction or another.

This paper has been typeset from a \LaTeX file prepared by the author.